RANS SIMULATIONS OF PLANE IMPINGING JETS: ON THE INFLUENCE OF PLATE VELOCITY IN THE NUSSELT NUMBER SECONDARY PEAK

Bruno A. C. Barata*, Jorge E. P. Navalho, José C. F. Pereira
IDMEC, Instituto Superior Técnico, Universidade de Lisboa, Lisboa, Portugal
*Corresponding author: bruno.a.c.barata@tecnico.ulisboa.pt

In the present work, heat transfer characteristics of a turbulent confined slot jet impinging on a heated moving plate are studied by means of time-averaged Navier-Stokes simulations. Three different plate conditions are considered: zero plate velocity (stationary plate); plate moving with a constant velocity; and plate moving with a constant acceleration. The jet nozzle-to-plate ratio and the jet inlet Reynolds number are equal to 4 *and* 2×10^4*, respectively. The objective of the present research is to investigate the role of the plate velocity condition on the development of the second peak in the Nusselt number profile along the impingement plate. The* k-kl-ω *transition RANS model was validated against DNS and experimental data and was able to correctly predict both the size and location of the Nusselt number secondary peak. A third recirculation zone appears as the plate velocity increases and the Nusselt number secondary peaks location shifts slightly downstream. The development of the third recirculation zone induces an accentuated decrease in the local and average Nusselt numbers. Furthermore, the plate acceleration delays the movement of the transition in the wall jets and the appearance of the third recirculation zone. Consequently, the average Nusselt number increases with time, and the heat transfer from the plate is enhanced up to* 8%*.*
Key words: Plane impinging jet, Confined jet, Moving flat plate, Heat transfer, RANS, Numerical simulation

1 Introduction

Confined impinging jets are used in industry for heat transfer enhancement in many engineering applications, such as electronic equipment [1, 2], in the drying process of materials [3, 4], and cooling turbine blades or combustion chambers [5]. Numerical predictions of the local heat transfer coefficient are required to accelerate the design process and, to this extent, the flow and thermal fields must be accurately and economically computed. A significant number of detailed reviews are available in literature – see *e.g.* [6–10].

The very large number of experimental and computational works dedicated to studying the flow and heat transfer of the turbulent impinging jet allows the enumeration of some of the most relevant findings to obtain accurate and economical simulations. Nowadays, it is well-known that impinging jet heat transfer is strongly affected by the jet nozzle-to-plate distance (H/B), being B the plane jet width or the circular jet diameter. For slot jets with high H/B (typically $H/B > 5$), the jet presents flapping oscillations [11]. The unsteady characteristics hinder accurate steady Reynolds-averaged Navier–Stokes (RANS) calculations [12]

and eddy-resolving simulations – large eddy simulation (LES) or hybrid RANS/LES – becomes required to capture the Kelvin-Helmholtz vortices for slot jets and the ring vortices for circular jets. This work is concerned with an H/B ratio equal to 4, and steady RANS models can still be satisfactorily applied avoiding the need for several orders of magnitude more expensive LES calculations.

Earlier studies of the Nusselt number distribution along the impinging plate reported the expected maximum heat transfer at the stagnation point and an unexpected maximum at approximately $r/B = 2$ for circular jets and $x/B = 7$ for slot jets – see the early works of Gardon and Akfirat [13] and Baughn and Shimizu [14]. The maximum heat transfer at the stagnation point and the intensity of the second Nusselt number peak depend on the Reynolds number and the H/B ratio. Ashforth-Frost *et al.* [15] experiments for $H/B = 4$, showed that the region with the highest turbulence levels is also where the Nusselt number increases, approaching the secondary peak. This indicates that transition to turbulence is complete beyond this region. On the other hand, this secondary peak is absent for $H/B = 9.2$. This behavior of the Nusselt number distribution is also observed for non-confined impinging jets – see *e.g.* Gardon and Akfirat [13]. As H/B is reduced below 8, two small "humps" start to appear at $x/B = \pm 7$, and for $H/B < 6$, they become well-defined second peaks in the heat transfer rate.

The Nusselt number secondary peak is fully detailed in eddy-resolving simulations. Jaramillo *et al.* [16] used direct numerical simulation (DNS) to study a turbulent plane impinging jet with an H/B ratio equal to 4 and at a Reynolds number of 2×10^4. Hattori and Nagano [17] have also employed DNS for H/B ratios from 0.5 to 2, and a Reynolds number of 10^4. Both DNS studies verified the existence of the mentioned second peak in the Nusselt number profile. Shukla and Dewan [18, 19] investigated the efficiency of LES in turbulent slot jet impingement heat transfer at $H/B = 4$ and for the Reynolds number of 2×10^4. Using four distinct sub-grid stress (SGS) models, the second peak in the Nusselt number profile was observed in good agreement with the experimental data. Additionally, Kubacki and Dick [12] demonstrated that the k-ω based hybrid RANS/LES model performs well at predicting the rate of heat transfer along the impingement plate and, in particular, it captures the dip in the Nusselt number profile.

Different explanations have been given to the occurrence of the wall Nusselt number secondary peak – see *e.g.* Viskanta [8], Uddin *et al.* [20]. For impinging circular jets, the detailed experiments of Grenson *et al.* [21] and the wall-resolved LES simulation by Gresson and Hugues [22] obtained with several hundred million mesh points explained how the small-scale hot spots are associated with the reattachment of local separations of the flow and streak structures, in line with Hadžiabdić and Hanjalic [23] LES simulations. According to Behnia *et al.* [24], the stagnation region is quasi-laminar, in the sense that the turbulent kinetic energy is relatively low and thus increases as the radial distance moves from the potential core to the wall jet region. The secondary peak for a circular jet impingement is not associated with a laminar to turbulent transition with increasing radius. For plane jets, according to Gardon and Akfirat [25], both the wall jet formation after the impingement and the disappearance of the pressure gradient that stabilizes the laminar boundary layer around the stagnation point are favorable conditions for the transition from a laminar to a turbulent boundary layer at the outer edge of the jet deflection region. The laminar to turbulent transition for the plane impinging jet was supported by eddy-resolving LES and DNS simulations – see *e.g.* [18, 26].

Many of the RANS turbulence models variants yield a physically unrealistic behavior of the Nusselt number on the impingement plate and do not predict the secondary peak – see *e.g.* [27, 28]. Computations of the impinging circular jet with the normal-velocity relaxation turbulence model ($v^2 - f$) [29, 30] are

in excellent agreement with the experimental results concerning the Nusselt number distribution and, in particular, the secondary peak. The excellent performance for the circular impinging jet may be associated with the new velocity variance scale v^2 (instead of turbulent kinetic energy) as a scale for turbulent transport. In addition, the $v^2 - f$ model uses an elliptic operator to compute a term analogous to the pressure-strain correlations. Concerning the plane jet, Jaramillo *et al.* [16, 31] compared several RANS models with the obtained DNS results and only the ARG ($k\omega$-LEVM) was able to replicate the Nusselt number findings downstream of the stagnation zone. The performance of several RANS turbulence models was also evaluated by Dutta and Dewan [32] for an H/B ratio equal to 4. The k-ω based models (standard and SST) with adjustments for transitional flow outperform the other models in terms of capturing the stagnation Nusselt number, position, and value of the secondary peak for small H/B ratios.

In conclusion, the turbulent flow structure in the vicinity of the Nusselt number secondary peak is well documented by DNS and wall-resolved LES for both circular and plane turbulent jets impinging on stationary plates. Despite these simulation tools being accurate and not presenting the limitations of the RANS modeling approach, they are not economical for industrial design purposes of enhanced heat transfer devices. Thus, significant improvements to the capabilities of RANS modeling have been made in the recent past – see *e.g.* Durbin [33] – and the selection and validation of RANS modeling will continue to evolve as the applications of CFD increase.

Regarding the case of a jet impinging on a plate moving at a constant velocity – as in the hot-rolling process –, the convective heat transfer is influenced by the splitted wall jet flow field that moves in the same or opposite direction of the moving plate. Heat transfer from jet impingement on a moving wall with $H/B = 3$ to 11 was presented by Raju and Schlünder [34]. The average heat transfer coefficients were verified to rise with the plate speed at first, reaching a maximum value, and then remaining almost constant at higher plate speeds. The maximal heat transfer coefficients were reported to be 1.5 to 2 times greater than the stationary plate case. Particle image velocimetry (PIV) was used by Senter and Solliec [35] to analyze the flow field structure of an isothermal slot jet impinging on a moving plate for $H/B = 8$. The flow field patterns reveled to be independent of the jet Reynolds number but dependent on the plate-to-jet velocity ratio (R). Several RANS studies were conducted to investigate the convective heat transfer from a moving hot plate due to confined slot jet impingement – see *e.g.* [36–41]. Overall, all studies concluded that the jet inlet Reynolds number has little effect on the flow field structure for a certain R ratio. Moreover, for small R ratios, the flow field is slightly modified, but for higher R ratios, the jet is significantly pushed. Additionally, it was observed that, for a particular value of R, the average Nusselt number increases with the jet Reynolds number and, with an increasing R ratio, the average Nusselt number initially decreases until a certain value (0.5 [36], 1 [40], 1.25 [39], and 1.5 [37, 38]) and then increases rather rapidly for the studied range. However, all these studies are focused on high H/B ratios, for which the second peak in the Nusselt number distribution is not present. Moreover, the simple case of a plane impinging jet on an isothermal hot flat plate under increasing velocity from zero to the desired velocity has not been investigated, as far as the authors are aware.

To this extent, the main objective of the present work is to investigate, by means of RANS, the influence of the plate velocity condition on the development of the Nusselt number secondary peak at the impingement plate, in order to close this present gap in the literature. To conduct this study, the jet nozzle-to-plate ratio and jet inlet Reynolds number were equal to 4 and 2×10^4, respectively. Particularly, this works aims to:

(i) assess the accuracy of different RANS turbulence models in predicting the Nusselt number secondary peak for impinging jets with a low H/B ratio;

(ii) analyze the effect of the plate velocity on the Nusselt number secondary peak and on the average heat transfer distribution along the impingement plate; and

(iii) analyze the effect of the plate acceleration on the flow field and Nusselt number secondary peak, in comparison with the case of constant plate velocity and fixed plate condition.

The paper is organized as follows: Section 2 presents the governing equations and the turbulence models used, as well as the numerical methods and boundary conditions. In Section 3, the performance of several RANS turbulence models is assessed and a set of results is presented for the cases of a plane jet impingement on a moving plate with constant or variable velocity, focusing on the heat transfer enhancement. The main conclusions of the study are provided in Section 4.

2 Mathematical and numerical models

In this work, the flow field has been assumed to be two-dimensional, and the fluid (air) is incompressible with constant thermophysical properties. The calculations were carried out using FLUENT 16.2 solver with mass, momentum, and energy equations – for steady flow in a time average formulation (RANS) – given by Eqs. (1), (2), and (3), respectively:

$$\frac{\partial}{\partial x_i}\left(u_i\right) = 0 \tag{1}$$

$$\rho\frac{\partial}{\partial t}\left(u_i\right) + \rho\frac{\partial}{\partial x_j}\left(u_i u_j\right) = -\frac{\partial p}{\partial x_i} + \frac{\partial}{\partial x_j}\left[\mu\left(\frac{\partial u_i}{\partial x_j} + \frac{\partial u_j}{\partial x_i} - \frac{2}{3}\delta_{ij}\frac{\partial u_l}{\partial x_l}\right)\right] + \rho\frac{\partial}{\partial x_j}\left(-\overline{u_i' u_j'}\right) \tag{2}$$

$$\rho\frac{\partial T}{\partial t} + \rho\frac{\partial}{\partial x_i}\left(u_i T\right) = \frac{\partial}{\partial x_i}\left(\frac{\lambda}{c_p}\frac{\partial T}{\partial x_i} - \rho\overline{u_i' T'}\right) \tag{3}$$

The Reynolds stresses ($-\rho\overline{u_i' u_j'}$) and vector heat flux ($-\rho\overline{u_i' T'}$) must be modeled in order to close the RANS equations, according to the turbulence model. A common method to relate the Reynolds stresses to the mean velocity gradients employs the Boussinesq hypothesis [42], used in the k-ε and k-ω models, which calculates the turbulent viscosity (μ_t). For the turbulent heat flux, the isotropic eddy diffusivity formulation was used $-\rho\overline{u_i' T'} = \frac{\mu_t}{Pr_t}\frac{\partial T}{\partial x_i}$ with Pr_t being the turbulent Prandtl number.

Accordingly, to choose the most suitable turbulence model, a number of RANS turbulence models were taken into account and evaluated against existing impinging jet with heat transfer data. The following turbulence models were herein considered for comparison: realizable k-ε [43] with enhanced wall treatment (EWT); shear-stress transport (SST) k-ω [44]; reynolds stress model (RSM) [45] with EWT; transition SST k-ω [46]; and k-kl-ω transition [47]. More details of these models and their implementation in FLUENT can be found in Reference [48].

The convection and diffusion terms were discretized using a second-order scheme. For steady calculations, the solution was considered to attain convergence when the normalized residual of each variable was

lower than 10^{-6}. For transient simulations, an implicit temporal discretization scheme was used, and the time step was defined such that the maximum CFL in the domain was lower than 1.

Fig. 1 presents the computational domain of the present study. At the inflow, a uniform velocity profile (V_j) was specified based on the value of the Reynolds number ($Re = V_j B/\nu$, where B is the slot width). Moreover, the turbulence intensity and the Reynolds number at the inlet were set at 1% and 2×10^4, respectively, in accordance with the data presented in Reference [15]. The jet inlet was set at ambient temperature (300 K). Additionally, a non-slip boundary condition was applied at the walls of the computational domain. The confinement plate was considered adiabatic. The impingement plate moves at a velocity U_p, corresponding to the plate-to-jet velocity ratio defined as $R = U_p/V_j$. A higher temperature than the ambient one was imposed at the impingement plate (320 K), in line with experimental and DNS studies [15] [16]. Outflow conditions were applied at both outlet sections, assuming atmospheric pressure. The outlet sections were located at a distance equal to $100B$ from each other which is sufficient to avoid backflow issues in accordance with literature [16].

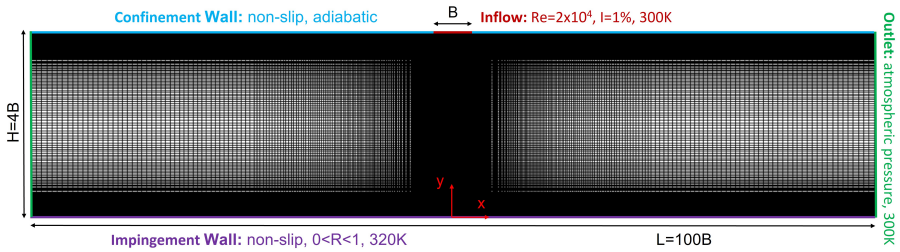

Figure 1: Schematic of the spatial discretization (mesh) of the computational domain.

A non-uniform mesh is required for the present study with grid points concentrated near the wall and around the jet centerline (see Fig. 1) to capture the strong gradients around the impingement region and high shear zones in the wall jet development. Four meshes were selected to conduct a grid convergence study: Mesh 1 ($61.5k$ cells); Mesh 2 ($123k$ cells); Mesh 3 ($246k$ cells); and Mesh 4 ($492k$ cells). Fig. 2 shows the distribution of the local Nusselt number – $Nu = -(\partial T/\partial y)_w \times B/(T_w - T_j)$ – along the (stationary) impingement plate between $0 < x/B < 12$ using the k-kl-ω transition model for the four meshes. It is observed that beyond Mesh 3 (820×300) no further significant change in the Nusselt number is noticed.

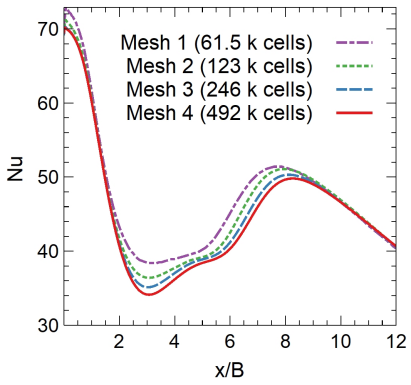

Figure 2: Nusselt number distributions for the four meshes.

Moreover, the spatial average Nusselt number over $-20 < x/B < 20$ calculated with the k-kl-ω transition model predicted 39.8, 39.4, and 39.2 for the Meshes 2, 3, and 4, respectively. The order of convergence p was estimated and the grid convergence index (GCI) [49] was computed for Mesh 3 and Mesh 4, considering a factor of safety of 1.25 since three grids were used to estimate p. The GCI for Mesh 3 and Mesh 4 is 0.0166 and 0.0094, respectively. Therefore, $\Lambda = 0.9947$ which is approximately 1 and the solutions are in the asymptotic range of convergence. Thus, Mesh 3 is able to describe the flow field virtually identically to a mesh with a higher cell density and Richardson extrapolation can be used for extrapolating the numerical solution. Consequently, this mesh is considered in all subsequent calculations.

3 Results

3.1 Stationary plate

The performance of several RANS turbulence models to predict the heat transfer from a impinging jet on a stationary plate is addressed in this subsection. Figs. 3 (a) and (b) show the distributions, in the range $0 < x/B < 12$, of the Nusselt number and the Nusselt number normalized by the stagnation Nusselt number, respectively. The results of the stated RANS turbulence models are compared with the DNS results from Jaramillo *et al.* [16] and the experimental results from Ashforth-Frost *et al.* [15]. The later set of benchmark results features a maximum Nusselt number of about 70 in the stagnation point and then a rapid drop to an off-stagnation minimum of about 35 ($0.5Nu_{st}$) at approximately $x/B = 3$ is observed. Beyond the off-stagnation minimum, the Nusselt number increases to a secondary maximum of about 50 ($0.69Nu_{st}$) at approximately $x/B = 7.4$, before decreasing monotonically with a further increase in x. On the other hand, the DNS results from Jaramillo *et al.* [16] show a peak of 63.4 at the stagnation point, an off-stagnation minimum of 25.9 ($0.41Nu_{st}$) at $x/B = 3.8$, and a secondary maximum of 45.7 ($0.72Nu_{st}$) at $x/B = 7.9$.

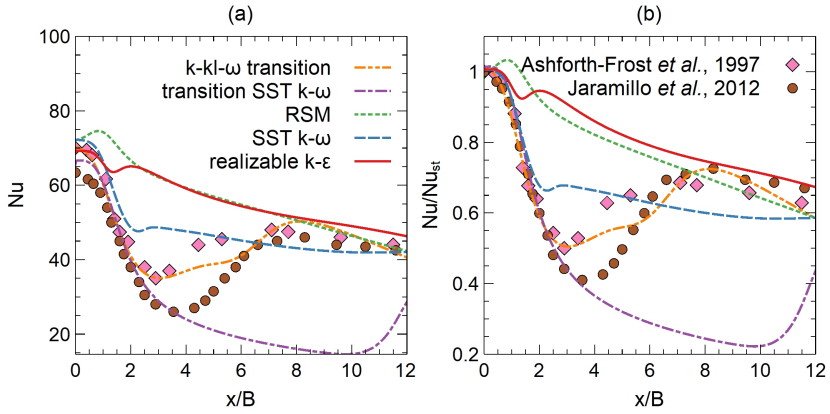

Figure 3: Distributions along $0 < x/B < 12$ of (a) Nusselt number and (b) Nusselt number normalized by the stagnation Nusselt number.

Regarding the performance analysis of the RANS turbulence models for a plane impinging jet, Fig. 3 (a) shows that all the studied models overpredict the Nusselt number at the stagnation point predicted by DNS. This evidence can be attributed to the role played by the jet inlet turbulence intensity (I) [32] since for the DNS study a value of 0.1% was considered while for the experimental and current results I was set equal to

1%. Moreover, the comparison with experimental results shows that both the RSM and the SST k-ω model overpredict the experimental value of the Nusselt number at the stagnation point, while the realizable k-ε and the k-kl-ω transition models match this parameter. Finally, the SST k-ω model with transitional flow modification underpredicts the Nusselt number at the stagnation point.

From Fig. 3 (b), it can be concluded that the RSM was not able to predict the second peak in the Nusselt number profile. Moreover, both the realizable k-ε and SST k-ω predict a slight dip (at $x/B \approx 1.4$ and $x/B \approx 2.3$, respectively) followed by a monotonic profile, instead of a prominent secondary peak. On the other side, when transitional flow modifications were considered, the SST k-ω model was able to predict the secondary peak, however, its location is shifted from about 7–$8B$ to $15B$ from the jet axis – not shown in Fig. 3 (b). Finally, the k-kl-ω transition model was able to correctly predict the Nusselt number secondary peak. Particularly, it shows an off-stagnation minimum of about $0.5Nu_{st}$ at $x/B \approx 3$, and a secondary maximum of about $0.71Nu_{st}$ at $x/B \approx 8$.

In conclusion, the RANS models adapted for transitional flow are able to predict the second peak in the Nusselt number profile. More concretely, the k-kl-ω transition model is able to correctly predict both the size and location of the secondary peak and, therefore, is considered in all subsequent calculations. In fact, the transition from laminar to turbulent conditions is responsible for the second peak in the Nusselt number distribution, being well predicted by transitional flow modifications. Hofmann *et al.* [50] and Dutta and Dewan [32] also found that using the transitional flow model results in improved predictions of the secondary peak, while Achari and Das [27] have reported the failure of RANS models without adjustments for transitional flow.

3.2 Moving plate with constant velocity

Regarding the case of a jet impinging on a moving plate, since the jet flow is split into two wall jets at the impingement and one of them flows in the plate movement direction and the other in the opposite direction, the impingement plate movement causes high shear zones that have severe impacts on fluid flow and thus the convective heat transfer will be influenced by the highly changed flow field. To study this effect, different plate-to-jet velocity ratios ($R = U_p/V_j$) have been considered. Figs. 4 (a)-(f) show the streamlines and the velocity magnitude plots for $R = 0, 0.2, 0.4, 0.6, 0.8$ and 1, respectively.

Fig. 4 (a) shows the typical flow field of a confined slot jet impinging on a stationary plate. Particularly, the flow field is symmetric about the jet axis, and two recirculation zones can be observed in the off-stagnation regions with centers at $|x/B| \approx 4.33$, due to both jet entrainment and the presence of the confinement wall. The left recirculation region (labeled as $A1$) is clockwise, and the right recirculation region (labeled as $A2$) is counterclockwise. The flow reattaches to the confinement wall at $|x/B| \approx 20.10$, reversing its direction. This reattachment length is in close agreement with the time-averaged DNS results reported by Jaramillo *et al.* [16] ($|x/B| \approx 22$).

When considering plate motion – positive in the x-direction –, the plate goes in the same direction as the right wall jet and in the opposite direction of the left one (in relation to the jet axis). This creates a rightward shear force on the fluid resulting in a distorted flow field with the jet deviating to the right. For $R = 0.2$ and 0.4 (Figs. 4 (b) and (c)), the impingement plate motion has a slight effect on the flow field, with the jet slightly deviating, moving the impingement point to $x/B \approx 0.10$ and $x/B \approx 0.25$, respectively.

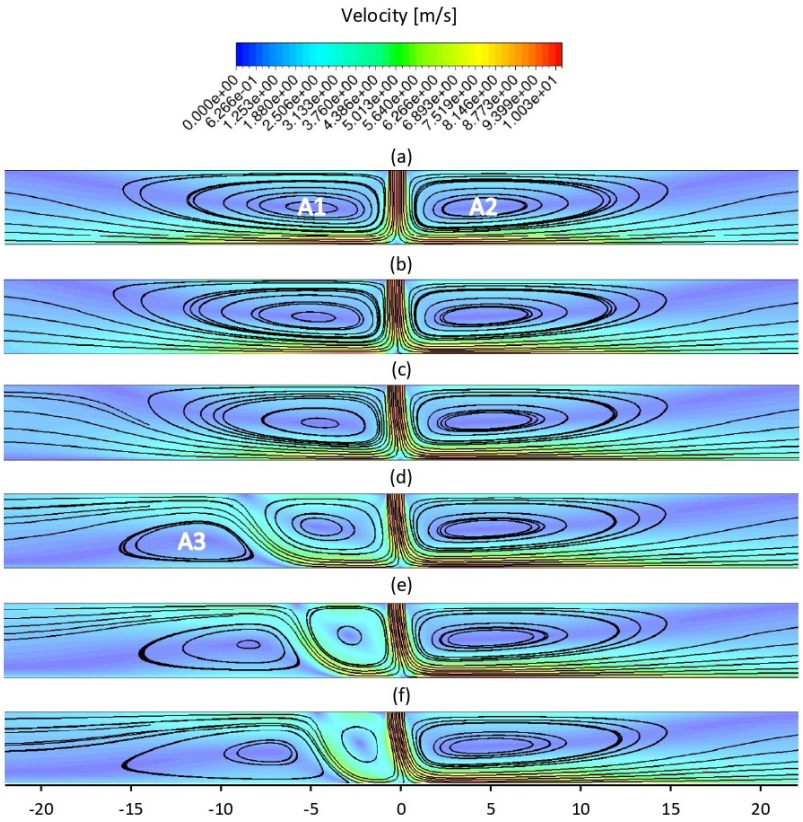

Figure 4: Velocity magnitude and streamline plots for (a) $\mathbf{R = 0}$, (b) $\mathbf{R = 0.2}$, (c) $\mathbf{R = 0.4}$, (d) $\mathbf{R = 0.6}$, (e) $\mathbf{R = 0.8}$, and (f) $\mathbf{R = 1}$.

For $R = 0.6$ (Fig. 4 (d)), the flow field is highly affected due to the appearance of a detachment point at $x/B \approx -5.08$, inducing the development of a secondary recirculation zone (labeled as $A3$) with center at $x/B \approx -10.76$ and with a rotation opposite to that of the recirculation zone $A1$. The detachment point is the result of the moving plate retarding the left wall jet. The recirculation zone $A3$ shifts the recirculation zone $A1$ towards the jet axis with its center at $x/B \approx -3.36$ and the jet is even more deviated (the stagnation point moves to $x/B \approx 0.3$). From this plate-to-jet velocity ratio onward, the flow field is highly asymmetric and an increase in R continues to deviate the impingement point, the recirculation zones, and the detachment point to the right. In particular, for $R = 0.8$ (Fig. 4 (e)), the left wall jet detachment is observed at $x/B \approx -2.86$ resulting in movement of recirculation zone $A3$ (centered at $x/B \approx -7.85$) towards the jet axis, squeezing the recirculation zone $A1$ (centered at $x/B \approx -2.31$). For $R = 1$ (Fig. 4 (f)) the detachment is located at $x/B \approx -1.85$ and the recirculation zones $A3$ and $A1$ are centered at $x/B \approx -6.78$ and $x/B \approx -1.79$, respectively.

The modifications on the flow field captured in Figs. 4 (a)-(f) highly affect the temperature distribution inside the channel and consequently the heat transfer at the impingement plate. (Temperature becomes less uniform close to the jet axis as R increases – not shown.) The variation of the local Nusselt number along $-20 < x/B < 20$ is shown in Fig. 5 (a) for $R = 0, 0.1, 0.2, 0.3, 0.4$, and 0.5 and for $R = 0, 0.6, 0.7, 0.8, 0.9$, and 1 in Fig. 5 (b). Moreover, the effect of the R ratio in the spatial average Nusselt number – $\langle Nu \rangle = 1/(2 \cdot x/B) \int_{-x/B}^{x/B} Nu(x)\, dx$ – over $-20 < x/B < 20$ is presented in Fig. 5 (c).

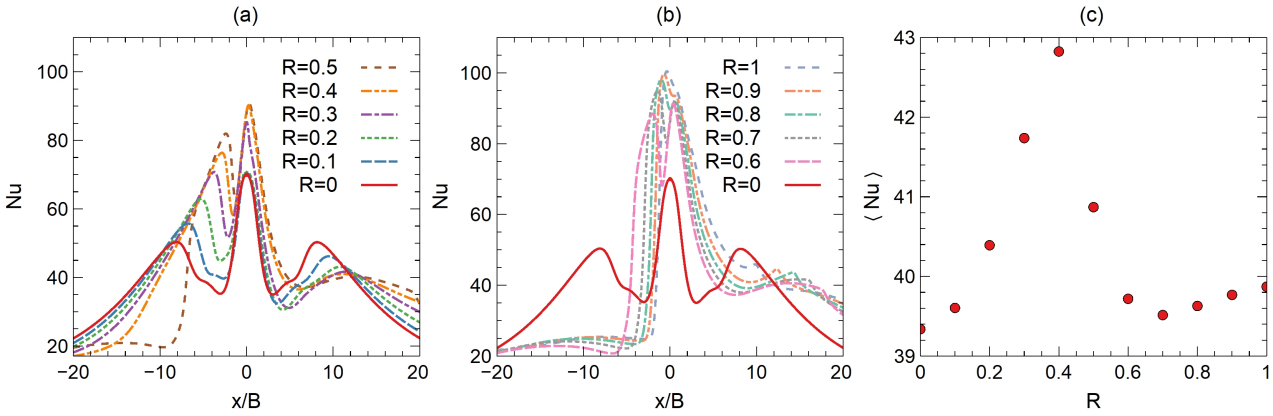

Figure 5: Nusselt number distribution along $-20 < \mathbf{x/B} < 20$ for (a) $\mathbf{R} = 0, 0.1, 0.2, 0.3, 0.4, 0.5$ and (b) $\mathbf{R} = 0, 0.6, 0.7, 0.8, 0.9, 1$, and (c) spatial average Nusselt number over $-20 < \mathbf{x/B} < 20$.

Firstly, for $R = 0.1$ and 0.2, the overshoot of the Nusselt number near the jet impingement point remains almost constant since the flow field is nearly unchanged for these plate-to-jet velocity ratios. However, it is notable that both secondary peaks move in the same direction of the plate velocity. This is observed because the transition from laminar to turbulent boundary layers is delayed or anticipated, depending on the wall jet flow going in the same or opposite direction as the moving plate, respectively. Furthermore, if the transition is anticipated (delayed), the value of the Nusselt number secondary peak increases (decreases).

With an increased R ratio, it is notable that the stagnation Nusselt number increases. This can be explained by the fact that, for the considered H/B ratio, the impingement plate is located within the potential core of the jet while in the previous studies, the impingement plate was placed in the developing region of the jet. Zhou and Lee [51] and Souris *et al.* [52] concluded that, for a jet impinging on a stationary plate, the stagnation Nusselt number increases up to $H/B = 6$ – by the rise in turbulence on the jet axis towards the plate direction – and then it decreases. With the increased plate velocity, the jet gets more deviated, and the "length" of the jet is extended, resulting in an increase of the stagnation Nusselt number for $H/B < 6$ and a decrease for $H/B > 6$. Moreover, from $R = 0.5$ onward, a remarkable decrease of the Nusselt number at the left side of the jet axis is observed and a further increase in the R ratio increases the size of the region where such decrease is registered. This decrease is related to the formation of the recirculation zone $A3$, as previously mentioned. From $R = 0.7$ onward, as the left wall jet transition gets increasingly anticipated, the left second peak in the Nusselt number profile increases up to a point that it gets higher than the stagnation Nusselt number. Furthermore, as notable for $R = 1$, the left secondary peak merges with the stagnation Nusselt number, and, from this point onward, the jet is effectively turbulent at the stagnation point due to the development of the jet before the impingement.

Additionally, Fig. 5 (c) shows that the average Nusselt number on the plate increases up to $R = 0.4$. This increase is attributed to both the increase of the value of the left secondary peak and to the increase of the stagnation Nusselt number. However, as previously mentioned, at $R = 0.5$ the recirculation zone $A3$ appears, which induces a decrease of the Nusselt number at the left side of the jet axis resulting also in a decrease in the average Nusselt number. Finally, despite the increase in the size of the region where this local decrease in the Nusselt number occurs (due to the recirculation zone $A3$), from $R = 0.7$ onward, the average

Nusselt number starts to increase. This is observed because the increase of both the left secondary peak and the stagnation Nusselt number is able to compensate for the aforementioned decrease in the left side of the jet axis. In general, the previous literature reported that the average Nusselt number initially decreases until a certain value, attaining a minimum, and then increases. However, all these studies are focused on high H/B ratios, where the second peak in the Nusselt number distribution is not present. Consequently, the presence of the Nusselt number secondary peak induces a quite different average Nusselt number evolution with R.

3.3 Moving plate with constant acceleration

In this subsection, the effect of the plate acceleration ($\partial U_p/\partial t$) in the flow field and heat transfer is analyzed. As an example, three different plate acceleration values are considered: 2.5, 5, and 10 $\mathrm{m/s^2}$. At $t = 0$ the solution for the stationary impinging plate is prescribed. The temporal study evolves from $t = 0$ (plate velocity $U_p = 0$) to $t_{\max}$ (plate velocity $U_p = V_j$, $R = 1$). Figs. 6 (a)-(c) show the velocity magnitude and streamlines plots at $R = 1$ for $\partial U_p/\partial t = 2.5$, 5, and 10 $\mathrm{m/s^2}$, respectively.

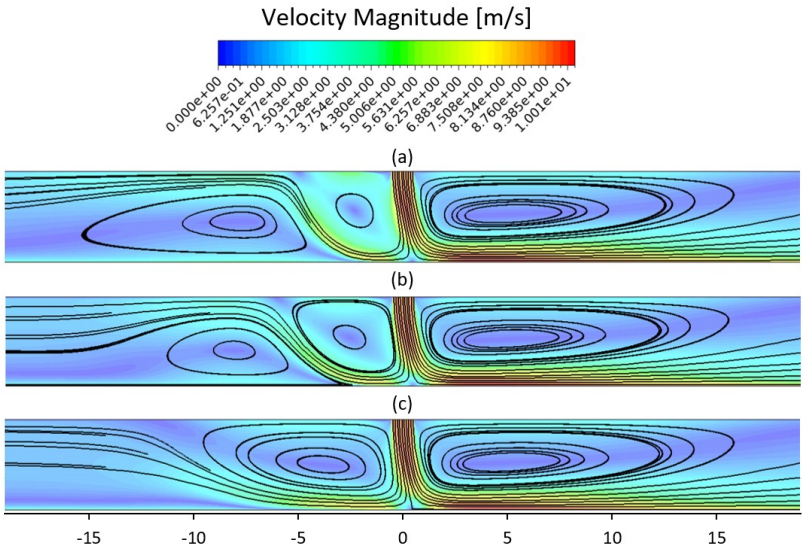

Figure 6: Velocity magnitude and streamline plots at $\mathbf{R = 1}$ for (a) $\partial \mathbf{U_p}/\partial \mathbf{t} = \mathbf{2.5\ m/s^2}$, (b) $\partial \mathbf{U_p}/\partial \mathbf{t} = \mathbf{5\ m/s^2}$, and (c) $\partial \mathbf{U_p}/\partial \mathbf{t} = \mathbf{10\ m/s^2}$.

In general, the comparison of Figs. 6 with Fig. 4 (f) shows the presence of the same flow characteristics. Particularly, the jet deviation to the right (in comparison with the case of a stationary plate), the movement of both recirculation zones, and the detachment point at the left wall jet. However, all these phenomena are delayed upon increasing plate acceleration. For example, when $U_p = V_j$ ($R = 1$) the impingement point is located at $x/B = 0.55$, 0.48, 0.46 and 0.41 for $\partial U_p/\partial t = 0$, 2.5, 5 and 10 $\mathrm{m/s^2}$, respectively. This delay has roots in the first-Stokes problem of the sudden acceleration of a laminar boundary layer and has also been reported in previous studies [53].

Additionally, with increasing acceleration, the detachment point of the left wall jet and the appearance of the recirculation zone $A3$ are only observed for higher R ratios. More concretely, for the accelerating plate with $\partial U_p/\partial t = 10$ $\mathrm{m/s^2}$ it is notable that the recirculation $A3$ does not appear – see Fig. 6 (c). Instead, it is only detectable the appearance of the detachment point of the left wall jet.

This temporal delay severely affects the amount of heat transfer and its distribution during the acceleration time. Fig. 7 (a) shows the Nusselt number distribution along $-20 < x/B < 20$ for $R = 0, 0.2$, and 0.4 while Fig. 7 (b) shows the Nusselt number distribution for $R = 0.6, 0.8$, and 1, considering the plate acceleration equal to $10\ \mathrm{m/s^2}$. Figs. 7 (a) and (b) also include the comparison with the case of the plate movement with the corresponding constant velocity. More concretely, the left column of the legend presents the profiles for the condition of constant plate velocity (also presented in Figs. 5 (a) and (b)) while the right column of the legend presents the profiles for the condition of constant plate acceleration.

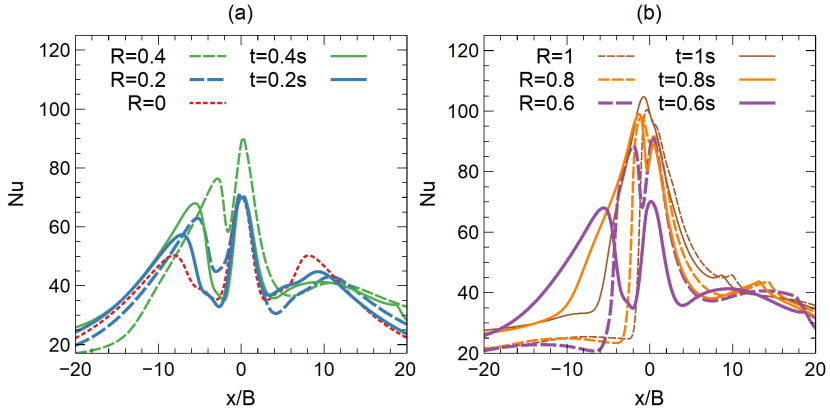

Figure 7: Nusselt number distribution for $\partial \mathbf{U_p}/\partial \mathbf{t} = \mathbf{10\ m/s^2}$ at (a) $\mathbf{R = 0, 0.2, 0.4}$ and (b) $\mathbf{R = 0.6, 0.8, 1}$. Solid lines: constant acceleration; dashed-lines: constant velocity conditions; and dotted line: stationary plate.

From Fig. 7 (a), it is notable that the plate acceleration also delays the location of the transition in both wall jets. Moreover, the overshoot of the Nusselt number near the jet impingement point does not increase when $R = 0.4$ ($t = 0.4$ s) since the jet is still nearly deviated. The delay in the appearance of the detachment point/recirculation zone $A3$ is also detectable in Fig. 7 (b), since the accentuated decrease of the Nusselt number at the left side of the jet axis only appears for higher R ratios.

The spatial average Nusselt number over $-20 < x/B < 20$ is presented in Figs. 8 (a), (b), and (c) for $\partial U_p/\partial t = 2.5$, 5 and $10\ \mathrm{m/s^2}$, respectively. The spatial average is obtained at each time step during the acceleration period – $\langle Nu \rangle|_t = 1/(2 \cdot x/B) \int_{-x/B}^{x/B} Nu(x,t)\ dx$ –, and is compared to the case of constant plate velocity. Up to $R = 0.4$ the plate acceleration presents nearly no effect on the average Nusselt number since the profiles match the points from the case of constant plate velocity. The verified slight difference (more notable for higher accelerations) is attributed to the difference in the stagnation Nusselt number and the location of the secondary peak. From $R = 0.4$ onward, the profiles exhibit an enormous difference. Since the appearance of the recirculation region $A3$ is delayed, the average Nusselt number – $\langle Nu \rangle|_t$ – continues to grow with an increasing R ratio. This growth also increases upon increasing the plate acceleration due to the increased delay. More concretely, the maximum spatial average Nusselt number is 44.09 (at $R = 0.55$), 45.06 (at $R = 0.68$), and 47.11 (at $R = 0.88$) for $\partial U_p/\partial t = 2.5$, 5 and $10\ \mathrm{m/s^2}$, respectively, correlating with $\langle Nu \rangle|_{\max} = 2.90{\times}10^7 (K \partial U_p/\partial t) + 42.82$, in which $K = \nu/U_j^3 = 1.5{\times}10^{-8}\ \mathrm{s^2/m}$. Thus, the spatial-temporal average Nusselt number over $-20 < x/B < 20$ from $R = 0$ to $R = 1$ – $\overline{\langle Nu \rangle} = 1/(2{\cdot}x/B{\cdot}\Delta t) \int_{-x/B}^{x/B} \int_0^{t_{\max}} Nu(x,t)\ dt\ dx$ – is 40.4 for $\partial U_p/\partial t = 0\ \mathrm{m/s^2}$, and 41.85, 42.74 and

43.55 for $\partial U_p/\partial t = 2.5$, 5 and 10 $\mathrm{m/s^2}$, respectively, clearly revealing the heat transfer enhancement with the plate acceleration, correlating with $\overline{\langle Nu \rangle} = -1.44 \times 10^{14}(K\partial U_p/\partial t)^2 + 4.26 \times 10^7 (K\partial U_p/\partial t) + 40.4$.

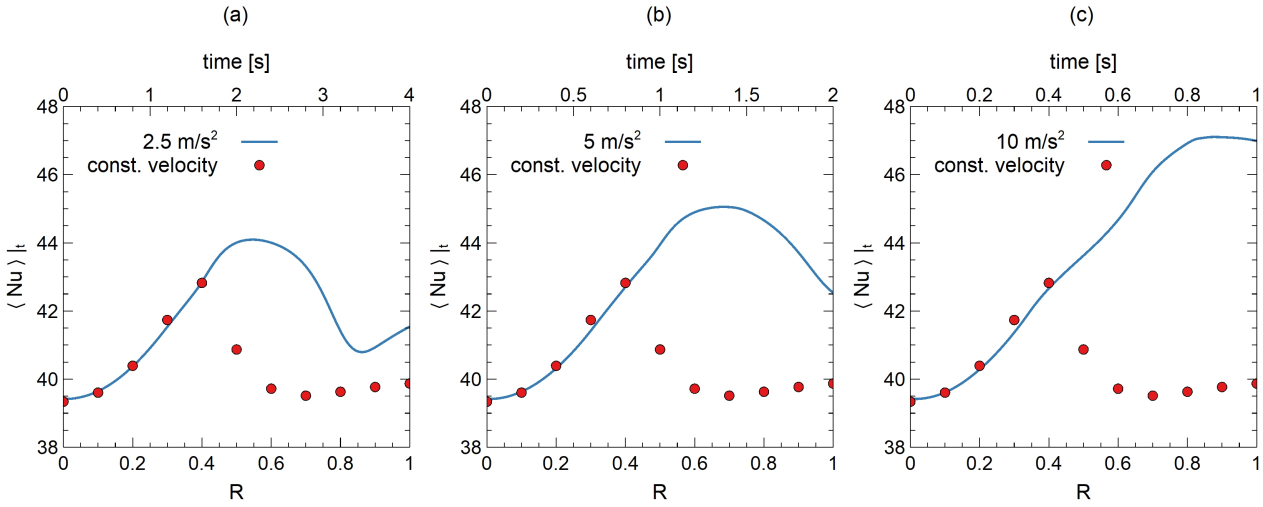

Figure 8: Spatial average Nusselt number over $-20 < \mathbf{x/B} < 20$ for (a) $\partial \mathbf{U_p}/\partial \mathbf{t} = 2.5\ \mathbf{m/s^2}$, (b) $\partial \mathbf{U_p}/\partial \mathbf{t} = 5\ \mathbf{m/s^2}$, and (c) $\partial \mathbf{U_p}/\partial \mathbf{t} = 10\ \mathbf{m/s^2}$.

Finally, it is important to highlight that if, after the acceleration time, the plate continued to move with constant $R = 1$ velocity, the average Nusselt number would recover (asymptotically) the value obtained for the constant plate velocity condition ($R = 1$), after a certain amount of time (depending on the plate acceleration). On the other side, if the plate started to decelerate with the same rate (negative) reaching the stationary plate state, the heat transfer would be prejudiced due to the non-disappearance of the third recirculation zone (not shown).

4 Conclusion

In this work, a turbulent slot jet impinging on a plate was considered with the objective to investigate numerically the influence of the plate velocity on the Nusselt number secondary peak. The classic case corresponding to the jet impingement on a fixed plate was used for validation of different RANS turbulence models. It was found that the k-kl-ω transition model is able to correctly predict both the size and location of the Nusselt number secondary peak.

Furthermore, with an increase in the plate-to-jet velocity ratio (R), it was verified that the secondary peaks moved in the direction of the plate velocity and the stagnation Nusselt number increased upon increasing the plate velocity, resulting in an increase of the average Nusselt number up to $R = 0.4$ (9% in comparison with $R = 0$). From $R = 0.5$ onward, a striking decrease of the local (at the left side of the jet axis) and average Nusselt number was observed due to the formation of a third recirculation zone.

Finally, the plate acceleration leads to a temporal delay of the jet evolution with the plate velocity, which increased upon increasing plate acceleration. Thus, the appearance of the third recirculation zone was delayed which implied that the average Nusselt number continued to grow with the R ratio. Consequently, the plate acceleration enhanced the overall heat transfer from the plate up to 8%.

Acknowledgements

This research was funded by the European Community's Framework Programme for Research and Innovation Horizon 2020 under grant agreement no. 768692 (ECCO). This work was also supported by FCT, through IDMEC, under LAETA, project UIDB/50022/2020.

Nomenclature

λ	Thermal conductivity, $[\mathrm{W/m \cdot K}]$
μ	Dynamic viscosity, $[\mathrm{kg/m \cdot s}]$
ν	Kinematic viscosity, $[\mathrm{m^2/s}]$
ρ	Density, $[\mathrm{kg/m^3}]$
B	Nozzle width, $[\mathrm{m}]$
c_p	Specific heat, $[\mathrm{J/kg \cdot K}]$
H/B	Nozzle-to-plate ratio, $[-]$
H	Channel height, $[\mathrm{m}]$
L	Length, $[\mathrm{m}]$
Nu	Local Nusselt number, $[-]$
p	Static pressure, $[\mathrm{Pa}]$; order of convergence, $[-]$
R	Plate-to-jet velocity ratio, $[-]$
Re	Reynolds number, $[-]$
T	Temperature, $[\mathrm{K}]$
t	Time, $[\mathrm{s}]$
u_i	Velocity, $[\mathrm{m/s}]$
U_p	Plate velocity, $[\mathrm{m/s}]$
V_j	Jet velocity, $[\mathrm{m/s}]$

References

[1] Koray Karabulut and Dogan Engin Alnak. Study of cooling of the varied designed warmed surfaces with an air jet impingement. *Pamukkale Univ Muh Bilim Derg*, 26(1):88–98, 2020.

[2] Koray Karabulut. Heat transfer improvement study of electronic component surfaces using air jet impingement. *Journal of Computational Electronics*, 18, 12 2019.

[3] D. Alnak and Koray Karabulut. Computational analysis of heat and mass transfer of impinging jet onto different foods during the drying process at low reynolds numbers. *Journal of Engineering Thermophysics*, 28:255–268, 04 2019.

[4] D. Alnak and Koray Karabulut. Analysis of heat and mass transfer of the different moist object geometries with air slot jet impinging for forced convection drying. *Thermal Science*, 22:2943–2953, 12 2018.

[5] B Han and R Goldstein. Jet-impingement heat transfer in gas turbine systems. *Annals of the New York Academy of Sciences*, 934:147–61, 06 2001.

[6] Holger Martin. Heat and mass transfer between impinging gas jets and solid surfaces. *Advances in Heat Transfer*, 13: , 12 1977.

[7] K. Jambunathan, Eliza Lai, M.A. Moss, and B.L. Button. A review of heat transfer data for single circular jet impingement. *International Journal of Heat and Fluid Flow*, 13:106–115, 06 1992.

[8] R. Viskanta. Heat transfer to isothermal gas and flame jets. *Experimental Thermal and Fluid Science*, 6:111–134, 02 1993.

[9] N Zuckerman, Noam Lior, and I Summary. Jet impingement heat transfer: Physics, correlations, and numerical modeling. *Advances in Heat Transfer*, 39: , 12 2006.

[10] Giovanni Carlomagno and Andrea Ianiro. Thermo-fluid-dynamics of submerged jets impinging at short nozzle-to-plate distance: A review. *Experimental Thermal and Fluid Science*, 58: , 10 2014.

[11] Bruno Barata, Jorge Navalho, and José Pereira. Prediction of self-sustained oscillations of an isothermal impinging slot jet. *Fluids*, 8:15, 12 2022.

[12] Slawomir Kubacki and Erik Dick. Simulation of plane impinging jets with k-ω based hybrid RANS/LES models. *International Journal of Heat and Fluid Flow*, 31:862–878, 10 2010.

[13] Robert Gardon and J. Akfirat. Heat transfer characteristics of impinging two-dimensional air jets. *Journal of Heat Transfer*, 88:101, 02 1966.

[14] J.W. Baughn and S. Shimizu. Heat transfer measurements from a surface with uniform heat flux and an impinging jet. *Journal of Heat Transfer (Transactions of the ASME (American Society of Mechanical Engineers), Series C); (United States)*, 111:4: , 11 1989.

[15] Shirley Ashforth-Frost, K. Jambunathan, and C.F. Whitney. Velocity and turbulence characteristics of a semiconfined orthogonally impinging slot jet. *Experimental Thermal and Fluid Science*, 14:60–67, 01 1997.

[16] J. Jaramillo, F.Xavier Trias, A. Gorobets, Carlos David Perez Segarra, and A. Oliva. DNS and RANS modelling of a turbulent plane impinging jet. *International Journal of Heat and Mass Transfer*, 55: , 01 2012.

[17] Hirofumi Hattori and Yasutaka Nagano. Direct numerical simulation of turbulent heat transfer in plane impinging jet. *International Journal of Heat and Fluid Flow*, 25:749–758, 10 2004.

[18] Anuj Shukla and Anupam Dewan. OpenFOAM based LES of slot jet impingement heat transfer at low nozzle to plate spacing using four SGS models. *Heat and Mass Transfer*, 00:1–21, 03 2019.

[19] Anuj Shukla and Anupam Dewan. Flow and Thermal Characteristics of Jet Impingement on a Flat Plate for Small Nozzle to Plate Spacing using LES. *International Journal of Thermal Sciences*, 145:1–17, 07 2019.

[20] Naseem Uddin, Olaf Neumann, and Bernhard Weigand. LES simulations of an impinging jet: On the origin of the second peak in the Nusselt number distribution. *International Journal of Heat and Mass Transfer*, 57:356–368, 01 2013.

[21] Pierre Grenson, Olivier Léon, Philippe Reulet, and Bertrand Aupoix. Investigation of an impinging heated jet for a small nozzle-to-plate distance and high reynolds number: An extensive experimental approach. *International Journal of Heat and Mass Transfer*, 102:801–815, 11 2016.

[22] Pierre Grenson and Deniau Hugues. Large-eddy simulation of an impinging heated jet for a small nozzle-to-plate distance and high reynolds number. *International Journal of Heat and Fluid Flow*, 68: , 11 2017.

[23] Muhamed Hadžiabdić and Kemal Hanjalic. Vortical structures and heat transfer in a round impinging jet. *Journal of Fluid Mechanics*, 596:221 – 260, 01 2008.

[24] M. Behnia, S. Parneix, and Paul Durbin. Prediction of heat transfer in an axisymmetric turbulent jet impinging on a flat plate. *International Journal of Heat and Mass Transfer*, 41:1845–1855, 06 1998.

[25] Robert Gardon and J.Cahit Akfirat. The role of turbulence in determining heat transfer characteristics of impinging jets. *International Journal of Heat and Mass Transfer*, 8:1261–1272, 10 1965.

[26] M. Duponcheel and Yann Bartosiewicz. Direct numerical simulation of turbulent heat transfer at low prandtl numbers in planar impinging jets. *International Journal of Heat and Mass Transfer*, 173:121179, 07 2021.

[27] A. Achari and Manab Das. Application of various rans based models towards predicting turbulent slot jet impingement. *International Journal of Thermal Sciences*, 98:332–351, 12 2015.

[28] Karel Petera and Martin Dostál. Heat transfer measurements and cfd simulations of an impinging jet. *EPJ Web of Conferences*, 114:02091, 03 2016.

[29] Paul Durbin. Application of a near-wall turbulence model to boundary layers and heat transfer. *International Journal of Heat and Fluid Flow*, 14:316–323, 12 1993.

[30] Paul Durbin. Near-wall turbulence closure modeling without damping function. *Theoretical and Computational Fluid Dynamics*, 3:1–13, 09 1991.

[31] J. Jaramillo, Carlos David Perez Segarra, Ivette Rodriguez, and A. Oliva. Numerical Study of Plane and Round Impinging Jets using RANS Models. *Numerical Heat Transfer, Part B: Fundamentals*, 54:213–237, 08 2008.

[32] Rabijit Dutta and Anupam Dewan. Comparison of various integration to wall (ITW) RANS models for predicting turbulent slot jet impingement heat transfer. *International Journal of Heat and Mass Transfer*, 65:750–764, 10 2013.

[33] Paul Durbin. Some recent developments in turbulence closure modeling. *Annual Review of Fluid Mechanics*, 50, 01 2018.

[34] K. Raju and E. Schlünder. Heat transfer between an impinging jet and a continuously moving flat surface. *Heat and Mass Transfer*, 10:131–136, 01 1977.

[35] Julien Senter and C. Solliec. Flow field analysis of a turbulent slot air jet impinging on a moving flat surface. *International Journal of Heat and Fluid Flow*, 28:708–719, 08 2007.

[36] Muhammad Sharif and A. Banerjee. Numerical analysis of heat transfer due to confined slot-jet impingement on a moving plate. *Applied Thermal Engineering*, 29:532–540, 02 2009.

[37] D. Benmouhoub and A. Mataoui. Turbulent heat transfer from a slot jet impinging on a flat plate. *Journal of Heat Transfer*, 135: , 10 2013.

[38] D. Benmouhoub and Amina Mataoui. Computation of heat transfer of a plane turbulent jet impinging a moving plate. *Thermal Science*, 18: , 01 2014.

[39] Mohammad Aghakhani. Heat transfer in a turbulent jet impinging on a moving plate considering high plate-to-jet velocity ratios. *Journal of Mechanical Science and Technology*, 28:4509–4516, 11 2014.

[40] D. Benmouhoub and A. Mataoui. Inclination of an impinging jet on a moving wall to control the stagnation point location. *International Journal of Thermal Sciences*, 89: , 03 2015.

[41] A. Achari and Manab Das. Conjugate heat transfer study of a turbulent slot jet impinging on a moving plate. *Heat and Mass Transfer*, 53: , 03 2017.

[42] J.O Hinze. *Turbulence*. McGraw-Hill, 2nd edition edition, 1959.

[43] Tsan Hsing Shih, William Liou, Aamir Shabbir, Zhigang Yang, and Jiang Zhu. A New k-ε Eddy Viscosity Model for High Reynolds Number Turbulent Flows. *Computers & Fluids*, 24:227–238, 03 1995.

[44] F. Menter. Two-equation eddy-viscosity turbulence models for engineering applications. *AIAA Journal*, 32:1598–1605, 01 1994.

[45] Brian Launder, G. Reece, and W. Rodi. Progress in the development of a reynolds stress turbulence closure. *Journal of Fluid Mechanics*, 68:537 – 566, 04 1975.

[46] D.C. Wilcox. *Turbulence Modeling for CFD*. DCW Industries, 3rd edition edition, 2006.

[47] D. Walters and Davor Cokljat. A Three-Equation Eddy-Viscosity Model for Reynolds-Averaged Navier–Stokes Simulations of Transitional Flow. *Journal of Fluids Engineering-transactions of The Asme*, 130: , 12 2008.

[48] Ansys. Ansys Fluent Theory Guide. *ANSYS, Inc*, 2021.

[49] P.J. Roache. Perspective: A method for uniform reporting of grid refinement studies. *Journal of Fluids Engineering-transactions of The Asme*, 116:405–413, 09 1994.

[50] Herbert Hofmann, Rafael Kaiser, Matthias Kind, and Holger Martin. Calculations of steady and pulsating impinging jets - an assessment of 13 widely used turbulence models. *Numerical Heat Transfer Part B-fundamentals*, 51:565–583, 04 2007.

[51] D.W. Zhou and Sang-Joon Lee. Forced convective heat transfer with impinging rectangular jets. *International Journal of Heat and Mass Transfer*, 50:1916–1926, 05 2007.

[52] N.N. Souris, H. Liakos, and Maria Founti. Impinging jet cooling on concave surfaces. *AIChE Journal*, 50:1672 – 1683, 08 2004.

[53] Hajime Nakamura, Riku Saito, and Shunsuke Yamada. Delay in response of turbulent heat transfer against acceleration or deceleration of flow in a pipe. *International Journal of Heat and Fluid Flow*, 85:108661, 10 2020.

Submitted: 06.02.2023.

Revised: 11.04.2023.

Accepted: 16.04.2023.